Supplementary Information

Random Conical Tilt Reconstruction

To determine starting models for RNase P and RNase MRP, we collected pairs of tilted and untilted negatively stained particles (-55°, 0°, Philips CM200, 200 kV, 27,500 magnification, 2kx2k TVIPS CCD camera) for random conical tilt reconstruction (1). We selected 2,156 pairs of particle images for RNase P and 1,588 pairs for RNase MRP. The untilted particle images were aligned and classified (100 classes for RNase P and 80 classes for RNase MRP) and the tilted images were centered. For each class of the untilted images, a volume was calculated from the related tilted images using the tilt angle from the microscope and the in-plane rotation determined for the corresponding untilted particle image. Many classes gave consistent volumes, but showed flattening due to the staining and drying process. Matching volumes were combined and used as a reference in further projection matching of tilted and untilted particle images. More untilted particle images were added to the data giving a total (tilted + untilted) of 9,226 particle images for RNase P and 7,553 particle images for RNase MRP. The results are summarized in Figure S1. The final volumes do not show any indications of flattening and represent the initial class averages of the untilted particles well. The random conical tilt reconstructions established the absolute hand off the models and were reliable starting models for the refinement of the larger data set of cryo-negative stain images.

CTF-correction and normalization of particle images

For each micrograph, the ctf-parameters were determined with ctffind2 (2). Particle images were boxed with a box size of 160x160 pixels, 35.2x35.2 nm. For phase reversal the boxed particle images were padded to a box size of 600x600 pixels and the phases were reversed with Spider (3) using the ctf-parameters determined with ctffind2. After phase reversal, the grey values were normalized, the box size was reduced to 120x120 pixels and a smooth circular mask was applied.

Determination of orientations of cryo-negative stain images by projection matching

The orientations of particle images were determined by projection matching. During iterative refinement projection matching was carried out in 2 steps: First the global orientation of the particle images was determined by a coarse search. Therefore, the reference volume was low-pass filtered to exclude spatial frequencies > 1/ 3.5 nm^{-1} and projected in 10° steps using quasi-evenly spaced projection directions as determined by the VO EA option of Spider. Particle images were cross-correlated with each of the reference projections. Then the orientation of the reference projection with which the particle image had the highest cross-correlation was assigned as particle orientation. For the global search the AP SH option of Spider was used, which performs an exhaustive grid search for the in-plane rotation and the origin. Changes in the origin of the particles were limited to 9 pixels. As first starting

model the refined volumes of the random conical tilt reconstruction were used (see above).

The coarse search was followed by a finer search in 2° steps in a limited search range (+/- 20° around the previously determined orientation). In the finer search the reference volume was low-pass filtered to include all spatial frequencies up to the frequency, where the Fourier-shell correlation in the previous iteration dropped to 0.5. The filtered reference volume was projected in 2° steps. Particle images were correlated with each of the projections within the limited search range. For the limited search, the AP REF option of Spider was used. In the limited search the change in origin was restricted to 4 pixels (0.88 nm).

Calculation of image reconstructions

The data was split into 20 defocus groups. For each defocus group three three-dimensional maps were calculated using the BP 32F option of Spider, which does a back-projection interpolated in Fourier space. The maps were calculated from particle images showing correlations with the reference projections above a certain threshold value. Because the correlation strongly depends on the defocus, we used a dynamic cut-off, which was determined by a linear fit of the correlation values of all particle images in dependence of the defocus value. The threshold value was chosen to include approximately 80% of all particle images. Some orientations were more frequent than others giving rise to anisotropic resolution. To reduce this effect, we restricted the number of particles with similar orientations in the final reconstructions. A maximum of 180 (RNase P) or 220 (RNase MRP) particle images respectively, which correlated best to the same reference in the global search, was included.

The maps, which were calculated with BP 32F, represented either all particle images above the threshold criterion (full-map) or alternating halves of the set of particle images (A- and B-maps). The maps of the different defocus groups were weighted according to the relative particle numbers and added to the final maps (full-map, A-map and B-map). The Fourier-shell correlation (4) was determined between A- and B-maps.

For preparing the full-map as reference map for projection matching, the map was masked with a binary mask with smooth edges, which was slightly larger than the volume of the particle. This reduced the background noise in the reference projections.

Checking the consistency of the assignment of particle orientations in the global search

To test whether the determination of particle orientations during the global orientation search was consistent, we sub-classified particle images, which were assigned with the same Euler angles. Sub-classification of the aligned particles was done using the multivariate statistical analysis of IMAGIC (5). In general sub-classes were consistent with the reference projections (Figure S2). This suggested that the large majority of particle images was assigned with the correct Euler angles.

Supplementary Figures and Legends

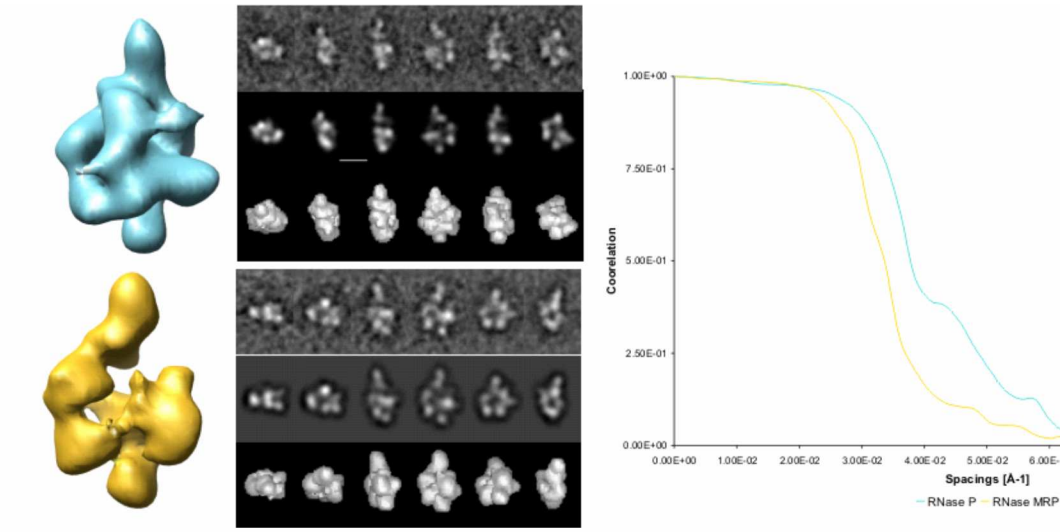

Figure S1. Initial reconstructions of RNase P (top) and RNase MRP (bottom). Left: surface representations are shown in a similar orientation. Centre: class averages from projection matching (top), projections of the volume in the same direction as determined for class averages (middle), surface representations of the volume viewed in the same direction as the projections (bottom). Right: Fourier shell correlation. The correlation drops to 0.5 at 1/27 $Å^{-1}$ for RNase P (blue) and 1/31 $Å^{-1}$ for RNase MRP (yellow).

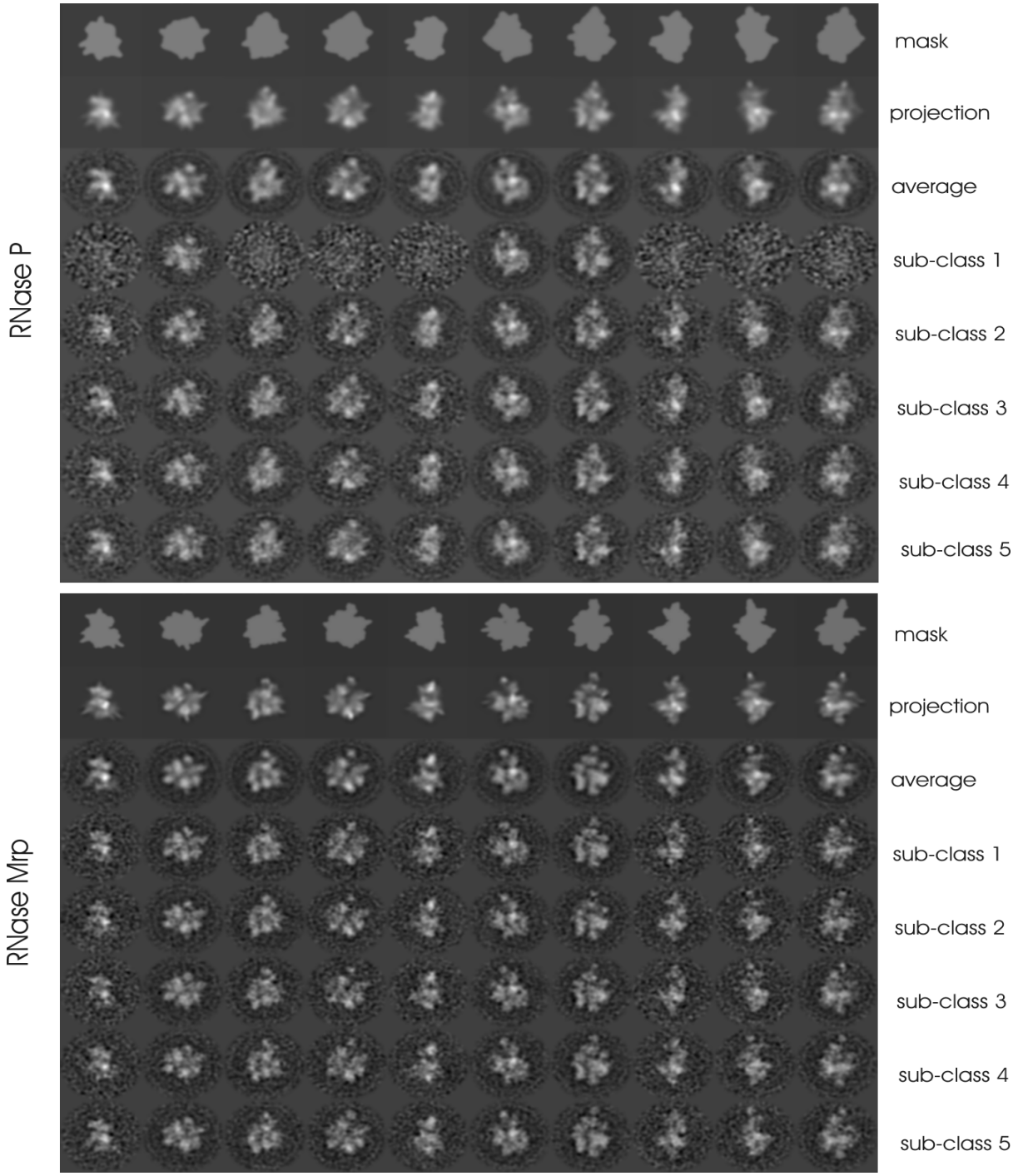

S2 Sub-classification of particles, which aligned to the same reference in the global orientation search. The upper panel shows RNase P, the lower panel shows RNase MRP. The analysis is shown for every 10th reference projection in the global search (columns 1-10). Row 1 shows the binary mask that was used in multivariate statistical analysis (6) in the sub-classification process. Row 2 shows the projection of the map, which were used as reference projections in the global search. Row 3 shows the average of all particles, which aligned best to the same reference projection in the global search. Reference projections (row 2) and averages (row 3) were similar highlighting the overall validity of the map.

Rows 4-8 show class averages of sub-classes of particles that aligned to the same reference in the global search. The classes were derived by multivariate statistical analysis. The majority of class averages are similar to the reference projection. This indicates that there are no systematic errors in the assignments of orientations and that there is very little heterogeneity in the data. This is consistent with observation from maximum-likelihood sorting using XMIPP (7). However, some of the less densely populated orientations contain images that do not represent particles and were accidentally included in the data set.

Figure S3 Surface representation of the map of RNase P (top panel) and RNase MRP (bottom panel) colored with the local correlation between the fitted atomic models and the EM-maps as shown in Figure 4 (the comparison also included Pop3 at the position indicated in Figure 4 by an arrow). The color-key for the correlation is given in the upper panel. White-blue colors represent cross-correlations >0.5 and white-yellow-red-colors cross-correlations < 0.5. The local cross-correlations were calculated within a distance of 1.1 nm (5 pixels) from the point of interest. For cross-correlation, the fitted models were converted to density maps and low-pass filtered to spatial frequencies of 1/1.7 nm^{-1} (RNase P) and 1/1.5 nm^{-1} (RNase MRP). The models do not represent density for Pop1, which explains the correlation

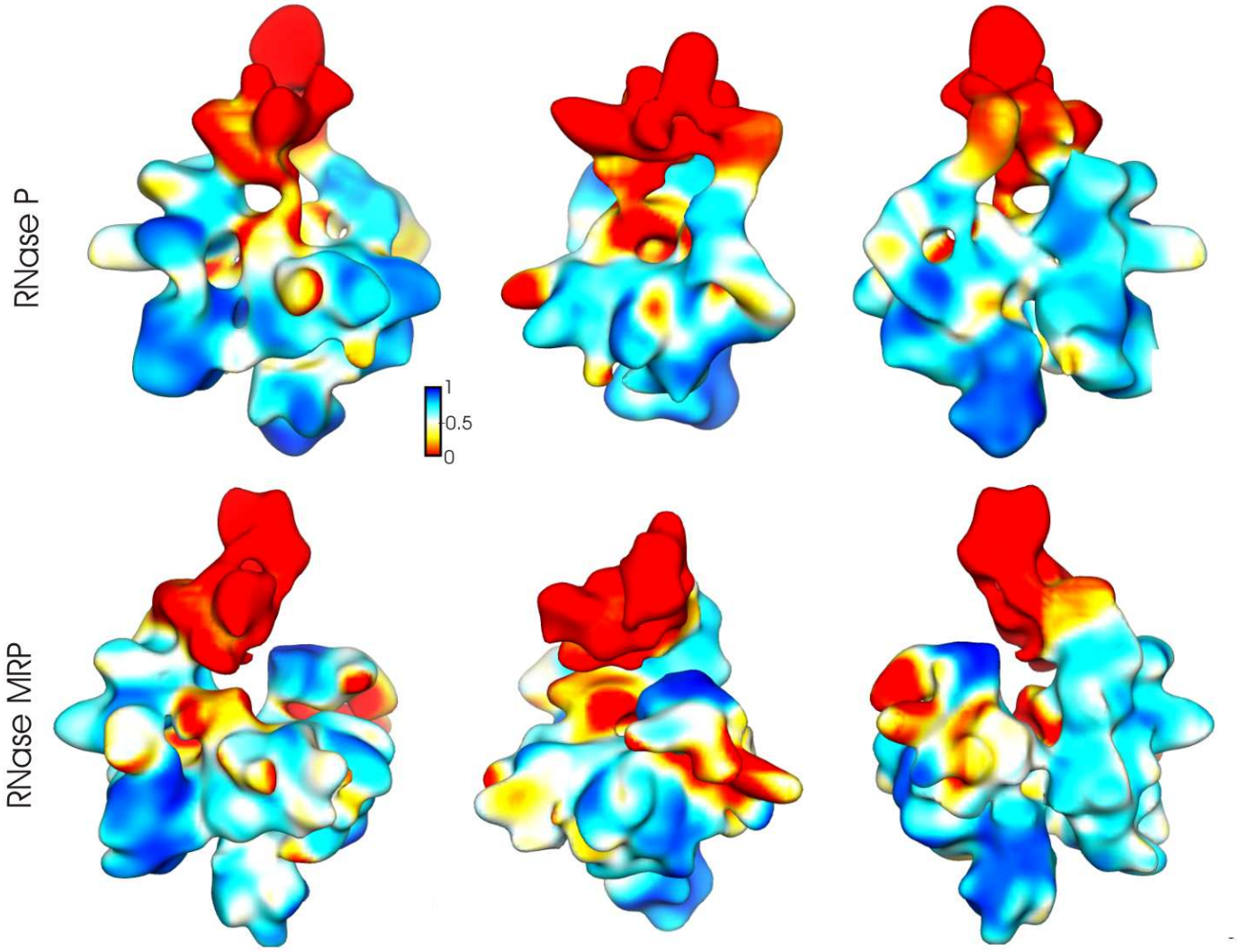

of 0 at the top of the particle.

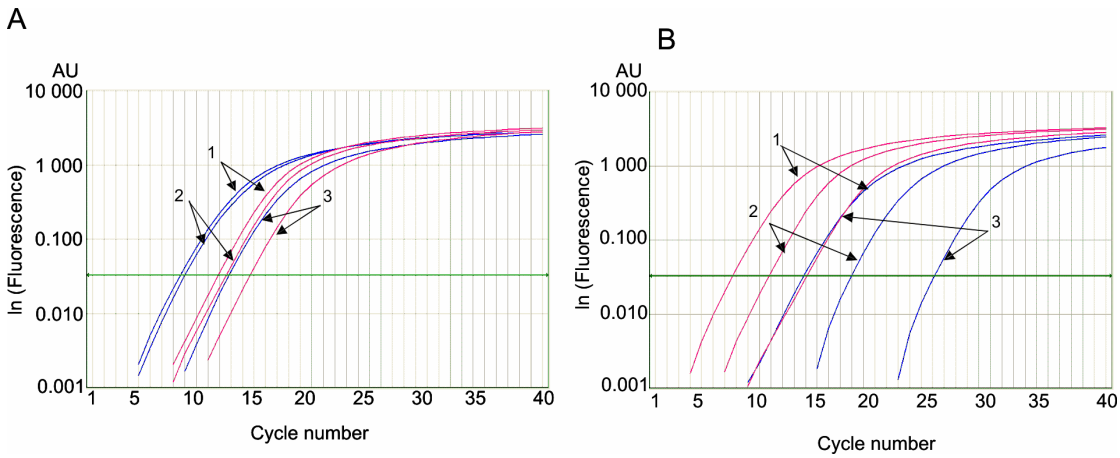

Figure S4. Logarithm of the fluorescence intensity over the number of cycles during qPCR of samples from three different purifications of RNase P and RNase MRP. (A) HA eluates of Pop4-TAP Rpr2-HA (RNase P) and (B) Pop4-TAP HA-Snm1 (RNase MRP). Red curves: Nme1 RNA (RNase MRP); blue curves: Rpr1 RNA (RNase P); green line: Ct threshold. The Δct ratios of Nme1 to Rpr1 were determined for three independent purifications (indicated by the arrows and numbers 1, 2 and 3). Amplification efficiencies were similar for both RNAs (ca. 92.5 %). For all purifications, there was at least 10 fold more Rpr1 than Nme1 for RNase P purifications and more than 50 fold Nme1 than Rpr1 for RNase MRP purifications.

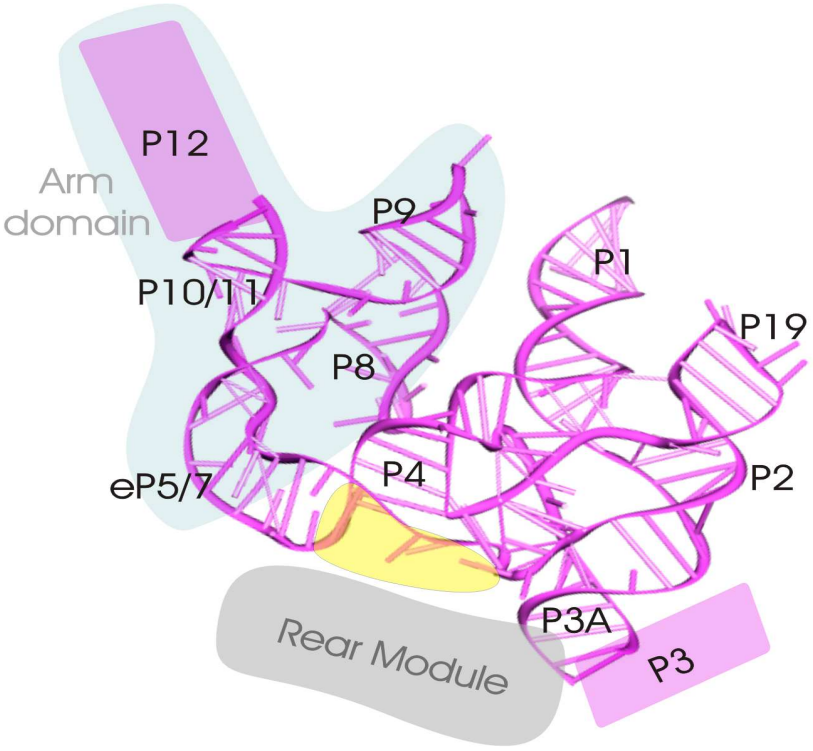

Figure S5 Cartoon of the model of the fitted *S. pombe* RNA (8) relative to the rear module. The RNA is viewed from the lid module towards the foot domain. The rear module and the approximate position of the arm domain are shown in grey. The approximate position of the catalytic site is shown in yellow. Larger stretches of RNA that are missing in the model are shown as boxes colored in magenta. The stems or the RNA model are labeled in black according to (8). The S-domain of the RNA-subunit is indicated by a light blue background.

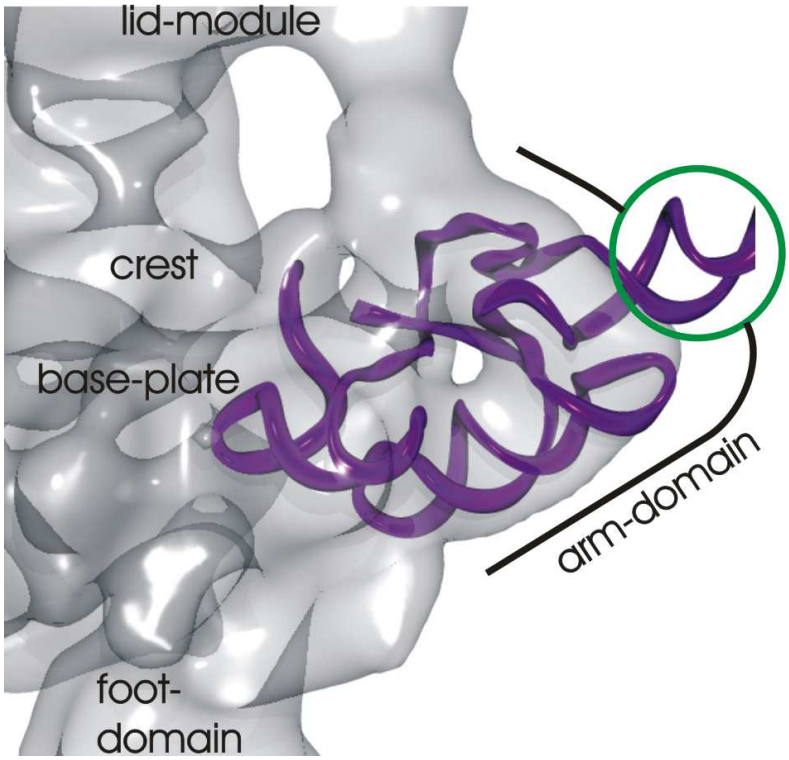

Figure S6 S-domain of the RNA-subunit of *Thermotoga maritima* ((9), purple) superimposed to the EM-map of the RNase P of *S. cerevisiae*. The subunit was placed manually. The green circle highlights an engineered region, which was introduced for optimizing crystal contacts and is not accommodated by the EM-density.

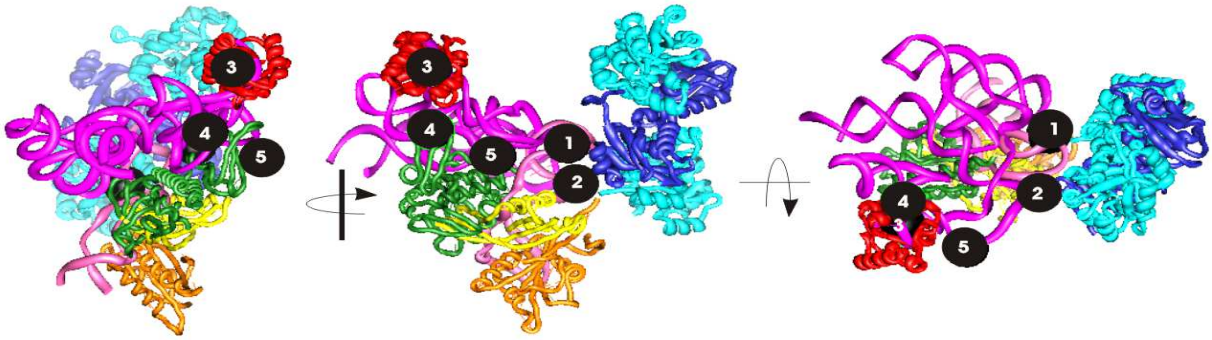

Figure S7 Model of RNase P as shown in Figure 4. The views are rotated by 90° around the axes as indicated. The black spheres have a diameter of 15Å and indicate positions of reported interactions that are consistent with our model: 1) interaction of P3a with the P3 stem bound to Pop6 and Pop7 (10) and interaction of the P3 stem with the Pop5-Rpp1 sub-complex (11). 2) Interaction of the P5 stem with Pop5-Rpp1 (11); 3) Interaction of the Pop3 homologue L7Ae with the P12-stem in Archaea (12). 4) Interaction of Pop4-Rpr2 with stems P9, P10 and P11 (11). 5) Snm1 in RNase MRP, which is homologous to Rpr2, is adjacent to the RNase MRP specific subunit Rmp1 (13). Position 5 highlights a region where the map of RNase MRP shows extra density, which is absent in the map of RNase P. For further details of the see also table S1.

Table S1 Summary of the evidence that supports the assignment and fitting of the subunits in the map and an estimation of the accuracy of the fits of the individual subunits and sub-complexes

subunit /sub-complex	**Evidence for the positioning**	**Estimated accuracy of the orientation of the fitted subunit/ sub-complex**	**comment**
Pop6-Pop7-P3	shape similarity of crystal structure (10) and map (this study) specific binding of Pop6 and Pop7 to the the P3 stem (14) (Figure S7, position 1) labeling (this study)	unique fit to the foot domain	
Pop5-Rpp1	shape similarity between the crystal structure of the homologous $(Ph1871\text{-}Ph1481)_2$ (15) with the rear module (the rear module is the only pseudo 2-fold symmetrical entity of the EM-density map) consistent with labeling (this study) archaeal Pop5-Rpp1 homologues bind to the C-domain of the respective RNA-subunit (16) (Figure S7, positions 1 and 2) foot-printing of archaeal homologues to the stems P3 and P5 (Figure S7) of the respective RNA-subunit (11) (Figure S7, positions 1 and 2)	unique fit to the rear module	one Pop5 might be exchanged for a Pop8 as suggested by the evolutionary relation between Pop5 and Pop8 (17) and as also consistent with labeling (this study)

RNA subunit	orientation relative to the P3 stem in the foot domain (Figure S7, interaction 1) foot-printing of archaeal homologues of Pop5-Rpp1 to stems P3 and P5 (11) support the relative orientation of the rear module to the RNA-subunit (Figure S7, positions 1 and 2)	some rotational freedom (<50°,mainly out of plane tilt of the RNA subunit) small positional freedom (<10Å)	
Pop3	In archaea Pop3 is replaced by L7Ae (12) which binds kink-turn motifs. These kink-turn motifs are preserved in the P12 stem of the RNA-subunit (12) (Figure S7, position 3).	full rotational freedom and small shifts (<10 Å) inside the arm module; therefore not included in the fit shown in Figure 4	
Rpr2-Pop4	consistent with labeling (this study) elongated shape of the crystal structure of the homologous Rpp21-Rpp29 (18) matches the unaccounted density underneath the base plate in the EM-map the archaeal Rpr2-Pop4 homologues bind to the S-domain of the respective RNA-subunit (16) (Figure S7, position 4) foot-printing of archaeal homologues to stems P9, P10, P11 and P12 of the respective RNA-subunit (11), (Figure S7, position 4) in RNase MRP the Rpr2 homologue Snm1	some rotational freedom mainly around the long axis of the Pop4-Rpr2-heterodimer (<40°) and small positional freedom (<10 A)	

	interacts with Rmp1 (13). This is consistent with the vicinity of the fitted Rpr2 to the unaccounted extra density in the map of RNase MRP (this study, Fig 2B *, Figure S7 position 5)		
Pop1	labeling (this study) the 100 $Å^3$ of the lid module agrees approximately with a molecular weight of a 100 kDa protein		

Supplementary References

1. Radermacher, M., Wagenknecht, T., Verschoor, A. and Frank, J. (1987) 3-dimensional reconstruction from a single exposure, random conical tilt series applied to the 50S-risomal subunit of escherichia-coli. *J of Microscopy-Oxford*, **146,** 113-136.
2. Mindell, J.A. and Grigorieff, N. (2003) Accurate determination of local defocus and specimen tilt in electron microscopy. *J Struct Biol*, **142,** 334-347.
3. Frank, J., Radermacher, M., Penczek, P., Zhu, J., Li, Y., Ladjadj, M. and Leith, A. (1996) SPIDER and WEB: processing and visualization of images in 3D electron microscopy and related fields. *J Struct Biol*, **116,** 190-199.
4. Harauz, G. and Van Heel, M. (1986) Exact Filters for General Geometry 3-Dimensional Reconstruction. *Optik*, **73,** 146-156.
5. van Heel, M., Harauz, G. and Orlova, E.V. (1996) A new generation of the IMAGIC image processing system. *J Struct Biol*, **116,** 17-24.
6. van Heel, M. and Frank, J. (1981) Use of multivariate statistics in analysing the images of biological macromolecules. *Ultramicroscopy*, **6,** 187-194.
7. Scheres, S.H., Gao, H., Valle, M., Herman, G.T., Eggermont, P.P., Frank, J. and Carazo, J.M. (2007) Disentangling conformational states of macromolecules in 3D-EM through likelihood optimization. *Nat Methods*, **4,** 27-29.
8. Marquez, S.M., Chen, J.L., Evans, D. and Pace, N.R. (2006) Structure and function of eukaryotic Ribonuclease P RNA. *Mol Cell*, **24,** 445-456.
9. Reiter, N.J., Osterman, A., Torres-Larios, A., Swinger, K.K., Pan, T. and Mondragon, A. (2010) Structure of a bacterial ribonuclease P holoenzyme in complex with tRNA. *Nature*, **468,** 784-789.
10. Perederina, A., Esakova, O., Quan, C., Khanova, E. and Krasilnikov, A.S. (2010) Eukaryotic ribonucleases P/MRP: the crystal structure of the P3 domain. *EMBO J*, **29,** 761-769.
11. Xu, Y., Amero, C.D., Pulukkunat, D.K., Gopalan, V. and Foster, M.P. (2009) Solution structure of an archaeal RNase P binary protein complex: formation of the 30-kDa complex between Pyrococcus furiosus RPP21 and RPP29 is accompanied by coupled protein folding and highlights critical features for protein-protein and protein-RNA interactions. *J Mol Biol*, **393,** 1043-1055.
12. Cho, I.M., Lai, L.B., Susanti, D., Mukhopadhyay, B. and Gopalan, V. (2010) Ribosomal protein L7Ae is a subunit of archaeal RNase P. *Proc Natl Acad Sci U S A*, **107,** 14573-14578.
13. Aspinall, T.V., Gordon, J.M., Bennett, H.J., Karahalios, P., Bukowski, J.P., Walker, S.C., Engelke, D.R. and Avis, J.M. (2007) Interactions between subunits of Saccharomyces cerevisiae RNase MRP support a conserved eukaryotic RNase P/MRP architecture. *Nucleic Acids Res*, **35,** 6439-6450.
14. Perederina, A., Esakova, O., Koc, H., Schmitt, M.E. and Krasilnikov, A.S. (2007) Specific binding of a Pop6/Pop7 heterodimer to the P3

stem of the yeast RNase MRP and RNase P RNAs. *RNA*, **13,** 1648-1655.
15. Kawano, S., Nakashima, T., Kakuta, Y., Tanaka, I. and Kimura, M. (2006) Crystal structure of protein Ph1481p in complex with protein Ph1877p of archaeal RNase P from Pyrococcus horikoshii OT3: implication of dimer formation of the holoenzyme. *J Mol Biol*, **357,** 583-591.
16. Honda, T., Hara, T., Nan, J., Zhang, X. and Kimura, M. (2010) Archaeal homologs of human RNase P protein pairs Pop5 with Rpp30 and Rpp21 with Rpp29 work on distinct functional domains of the RNA subunit. *Biosci Biotechnol Biochem*, **74,** 266-273.
17. Rosenblad, M.A., Lopez, M.D., Piccinelli, P. and Samuelsson, T. (2006) Inventory and analysis of the protein subunits of the ribonucleases P and MRP provides further evidence of homology between the yeast and human enzymes. *Nucleic Acids Res*, **34,** 5145-5156.
18. Honda, T., Kakuta, Y., Kimura, K., Saho, J. and Kimura, M. (2008) Structure of an archaeal homolog of the human protein complex Rpp21-Rpp29 that is a key core component for the assembly of active ribonuclease P. *J Mol Biol*, **384,** 652-662.